

Bridging Elastic and Active Turbulence

Vedad Dzanic,^{1,*} Sumesh P. Thampi,^{2,†} and Julia M. Yeomans^{3,‡}

¹*School of Mechanical, Medical, and Process Engineering,
Queensland University of Technology, Brisbane, QLD 4001, Australia*

²*Department of Chemical Engineering,
Indian Institute of Technology Madras, Chennai 600036, India*
³*The Rudolf Peierls Centre for Theoretical Physics, Department of Physics,
University of Oxford, Parks Road, Oxford OX1 3PU, United Kingdom*

(Dated: January 15, 2026)

Remarkably, even under negligible inertia, the addition of microstructural agents can generate chaotic flow fields. Such behavior can arise in polymer solutions leading to *elastic turbulence*, or from active, self-driven particles, which generate *active turbulence*. Here, we demonstrate a close, hitherto unrecognized connection between these two classes of turbulence. Specifically, we reveal that the continuum descriptions are analogous at the macroscopic level, so that the polymeric fluids can be interpreted as a deformable analogue of contractile active matter. Moreover, our numerical results for the Kolmogorov flow demonstrate that the transition into the well-known traveling arrowhead structures in elastic turbulence is marked by the emergence of charge $\pm 1/2$ topological defects—long recognized as a defining feature of active turbulence—in the polymer director field. Importantly, these coherent structures originate from a transverse instability driven by activity-like gradients generated by anisotropically stretched, contractile polymers. At sufficiently strong activity the system undergoes a transition into a flow-suppressed state characterized by weak polymer stretching and ordering, a behavior that can be explained by analogy to the spontaneous-flow transition observed in channel-confined active nematics.

The classical understanding of turbulence is rooted in the dominance of inertial effects, characterized by high Reynolds numbers $Re \gg 1$, where strong, externally imposed forces give rise to chaotic flow dynamics marked by a cascade of energy from large to small scales. However, in recent decades, a new class of turbulence has emerged under inertialess conditions (i.e., $Re \ll 1$), where chaotic dynamics are instead sustained through internal stress contributions arising from microstructural agents. One such example can occur if long-chain, flexible polymers are added to a background fluid. The polymers are stretched and aligned by flow gradients, and their relaxation generates contractile elastic stress contributions that can transition the flow into a chaotic regime, coined *elastic turbulence* [1, 2]. Elastic turbulence is distinguished by increased flow resistance [3, 4], enhanced mixing [5, 6] and random flow fluctuations characterized by a broadband spectrum of spatial and temporal frequencies [3, 7, 8]. Recent studies [9, 10] have further revealed the presence of exact coherent structures in parallel shear flows. These take the form of traveling arrowhead-like patterns, arising from a center-mode instability [11], highlighting organized features within otherwise chaotic elastic turbulence.

Similar inertialess chaotic flows emerge in dense active nematic systems, which comprise self-driven disc-like or rod-like particles that continuously transform energy into motion. Examples include bacteria [12–14], microtubules driven by molecular motors [15, 16], and epithelial cells [17–19]. Because the particles are self-propelled, active nematics exert dipolar forces [20], and the resulting stresses drive a hydrodynamic instability that leads to a state commonly referred to as *active turbulence* [21, 22]. The

active turbulent state is characterized by a chaotic pattern of vortices, short-range nematic order, and the spontaneous creation, motion, and annihilation of topological defects [21, 22]—distinct patterns in the orientationally ordered constituents—whose dynamics play a central role in sustaining the chaotic flows [23–27].

In addition to both exhibiting low-Reynolds-number chaos [2, 21], active nematics and extended polymers share several other properties: they act as contractile hydrodynamic force dipoles, the continuum equations of motion describing their microstructural dynamics are written in terms of rank-2 order tensors [28, 29], and the two systems exhibit similar universal scaling properties [30–32]. A key difference, however, is that active turbulence can be driven by internal activity, whereas polymeric turbulence requires an imposed flow.

In what follows, we investigate the connection between the physical descriptions of elastic turbulence in polymeric systems and active turbulence in active nematics. We demonstrate a direct theoretical mapping from the constitutive equations of polymeric fluids to the analogous description for active nematics, which requires imposing the microstructural constraint of constant polymer extension. In this continuum picture, polymer stretching can be considered to generate an effective activity coefficient that varies in space and time. The correspondence further reveals nematic signatures exhibited by stretched polymers, and the flows that arise from the distortions in the nematic ordering of polymers. We highlight the link between topological defect pairs in the nematic ordering of stretched polymers and the distinctive arrowhead coherent structures observed for elastic turbulence [9–11, 33].

Moreover, the mapping motivates a hydrodynamic description for active nematics which allows for changes in the shape of the nematogens, important for many epithelial cells.

Section I of the paper introduces the equations of motion for a dilute polymeric fluid, and for active nematics, and describes the mapping between the polymers and driven, contractile active nematics. In Section II, we illustrate the connection by presenting numerical simulations of polymers under Kolmogorov (sinusoidal) forcing. Our analysis follows a three-step approach. We first keep the polymer extension fixed, corresponding to the active nematic limit. We then allow the polymer extension to vary in space, but not in time, which corresponds to allowing spatial variations in nematic activity. Finally we compare to solutions of the full polymeric equations, where the polymer extension evolves dynamically in both space and time. Section III summarizes and discusses our results.

I. COMPARING THE EQUATIONS OF MOTION OF POLYMERIC AND ACTIVE NEMATIC FLUIDS.

A. Equations of motion for a dilute suspension of polymers

To investigate their microstructure under flow, polymers are canonically represented by a space-time dependent, symmetric conformation tensor, \mathbf{C} , where $\text{tr}(\mathbf{C})$ is a measure of the polymer extension. The equation of motion of the conformation tensor is

$$\frac{D\mathbf{C}}{Dt} = \mathbf{S}_C - \frac{1}{\tau_p} (\mathbf{C} - \mathbf{I}) + \varepsilon \nabla^2 \mathbf{C}. \quad (1)$$

On the lhs of (1), $D \bullet / Dt = \partial_t \bullet + \mathbf{u} \cdot \nabla \bullet$ is the material derivative. The first term on the rhs is the generalized convected derivative

$$\mathbf{S}_C = \mathbf{C} \cdot (\nabla \mathbf{u}) + (\nabla \mathbf{u})^\top \cdot \mathbf{C} + (\lambda - 1)(\mathbf{C} \cdot \mathbf{E} + \mathbf{E} \cdot \mathbf{C}), \quad (2)$$

which describes the response of the polymers to velocity gradients where \mathbf{u} is the velocity field, \mathbf{E} is the strain rate tensor, and Ω (used below) is the vorticity tensor. λ is the flow aligning parameter which is introduced as a material dependent quantity describing the relative effects of strain rate and vorticity on the microstructure. The second term on the rhs of (1) models relaxation of the polymers to their unstretched state, which corresponds to the unit tensor \mathbf{I} , on a time scale τ_p . The final term is a diffusion term with coefficient ε [34–36].

The velocity field obeys the incompressible Navier-Stokes equations,

$$\nabla \cdot \mathbf{u} = 0, \quad \rho \frac{D\mathbf{u}}{Dt} = -\nabla P + \mu_s \nabla^2 \mathbf{u} + \nabla \cdot \boldsymbol{\sigma}_p + \rho F \hat{\mathbf{F}}, \quad (3)$$

where ρ , P , μ_s are respectively the density, pressure and solvent's dynamic viscosity, and $F \hat{\mathbf{F}}$ is an external driving force density of magnitude F along the unit vector $\hat{\mathbf{F}}$. The additional stress exerted on the fluid as the polymers relax towards equilibrium is

$$\boldsymbol{\sigma}_p = \frac{\mu_p}{\tau_p} (\mathbf{C} - \mathbf{I}), \quad (4)$$

where μ_p is the dynamic viscosity of the polymers [37, 38].

B. Equations of motion for active nematics

In a similar approach the microstructure of an active nematic is encoded by a symmetric traceless tensor,

$$\mathbf{Q} = 2S(\mathbf{n}\mathbf{n} - \mathbf{I}/2) \quad (5)$$

where S is the magnitude of the nematic order along a director \mathbf{n} which is the eigenvector corresponding to the largest eigenvalue of \mathbf{Q} . The equation of motion for \mathbf{Q} is

$$\frac{D\mathbf{Q}}{Dt} = \mathbf{S}^Q + \Gamma \mathbf{H}, \quad (6)$$

with a generalized co-rotational term

$$\mathbf{S}^Q = (\lambda \mathbf{E} + \Omega) \cdot (\mathbf{Q} + \mathbf{I}/2) + (\mathbf{Q} + \mathbf{I}/2) \cdot (\lambda \mathbf{E} - \Omega) - 2\lambda(\mathbf{Q} + \mathbf{I}/2)(\mathbf{Q} : \mathbf{E}). \quad (7)$$

The second term on the rhs of (6) describes the relaxation of the nematogens to the minimum of a free energy at a rate Γ . We choose a free energy [39]

$$\mathcal{F} = \frac{A}{2} \mathbf{Q}^2 + \frac{K}{2} (\nabla \mathbf{Q})^2, \quad (8)$$

where A is a material coefficient, which is taken to be positive to ensure that the system is in a paranematic (isotropic) state with $S = 0$ in the absence of activity [40]. K is the elastic constant, assuming the usual single elastic constant approximation. The molecular field is then

$$\mathbf{H} = -\frac{\delta \mathcal{F}}{\delta \mathbf{Q}} + \frac{I}{2} \text{tr} \left(\frac{\delta \mathcal{F}}{\delta \mathbf{Q}} \right) = -A\mathbf{Q} + K \nabla^2 \mathbf{Q}. \quad (9)$$

The velocity field for active nematics is described by (3), but with the polymer stress replaced by the sum of an active stress, $\boldsymbol{\sigma}_{\text{active}}$, created by the active dipolar forces produced by individual particles [20], together with a small elastic backflow term associated with the relaxation of the order parameter to the free energy minimum, which we will neglect. The active stress is

$$\boldsymbol{\sigma}_{\text{active}} = -\zeta \mathbf{Q}, \quad (10)$$

where ζ is the activity coefficient which quantifies the strength of the activity. $\zeta < 0$ corresponds to contractile activity, which will primarily concern us here, where the dipolar forces act inwards along a particle's axis of elongation; $\zeta > 0$ represents extensile activity, where the forces act outwards along the long axis.

C. Comparing polymer and active nematic hydrodynamics

The key difference between the conformation tensors \mathbf{C} and \mathbf{Q} is that the latter is traceless. Therefore we construct a normalized, traceless tensor, $\mathbf{C}^* = (\mathbf{C} - \text{tr}(\mathbf{C})\mathbf{I}/2)/\text{tr}(\mathbf{C})$, and decompose the polymer tensor into a traceless component, $\text{tr}(\mathbf{C})\mathbf{C}^*$, and a diagonal component, $\text{tr}(\mathbf{C})\mathbf{I}/2$ by writing

$$\mathbf{C} = \text{tr}(\mathbf{C})(\mathbf{C}^* + \mathbf{I}/2). \quad (11)$$

Substituting this expression into (1), some algebra, which is detailed in the Supplemental Material, we derive the following governing equations for \mathbf{C}^* and $\text{tr}(\mathbf{C})$:

$$\frac{D\mathbf{C}^*}{Dt} = \mathbf{S}^* - \frac{2}{\text{tr}(\mathbf{C})\tau_p}(\mathbf{C}^*) + \varepsilon \nabla^2 \mathbf{C}^* + \frac{2\epsilon}{\text{tr}(\mathbf{C})} \nabla \text{tr}(\mathbf{C}) \cdot \nabla \mathbf{C}^*, \quad (12)$$

where

$$\begin{aligned} \mathbf{S}^* = & (\lambda \mathbf{E} + \boldsymbol{\Omega}) \cdot (\mathbf{C}^* + \mathbf{I}/2) + (\mathbf{C}^* + \mathbf{I}/2) \cdot (\lambda \mathbf{E} - \boldsymbol{\Omega}) \\ & - 2\lambda(\mathbf{C}^* + \mathbf{I}/2)(\mathbf{C}^* : \mathbf{E}), \end{aligned} \quad (13)$$

$$\begin{aligned} \frac{D \text{tr}(\mathbf{C})}{Dt} = & 2\lambda \text{tr}(\mathbf{C}) (\mathbf{C}^* : \mathbf{E}) \\ & - \frac{1}{\tau_p} (\text{tr}(\mathbf{C}) - 2) + \varepsilon \nabla^2 (\text{tr}(\mathbf{C})). \end{aligned} \quad (14)$$

Comparing the microstructural evolution equations for \mathbf{C}^* , (12) and (13) in the rigid rod limit, $\text{tr}(\mathbf{C}) = \text{constant}$, with those for the nematic tensor, \mathbf{Q} , (6), (7) and (9), shows that they are identical if

$$-\Gamma A \mathbf{Q} \Leftrightarrow -\frac{2}{\text{tr}(\mathbf{C})\tau_p}(\mathbf{C}^*), \quad (15)$$

$$\Gamma K \nabla^2 \mathbf{Q} \Leftrightarrow \varepsilon \nabla^2 \mathbf{C}^*. \quad (16)$$

Similarly, the equations of motion for the velocity fields of the two tensors map onto each other if the deviatoric part of the polymeric and active stresses, (4) and (10), are related by

$$-\zeta \mathbf{Q} \Leftrightarrow \frac{\mu_p}{\tau_p} (\text{tr}(\mathbf{C})\mathbf{C}^*). \quad (17)$$

Thus the polymer equations map onto those of active nematics if (14) can be neglected, i.e. if $\text{tr}(\mathbf{C})$ is held constant.

Before presenting numerical results demonstrating the connection between elastic and active low Reynolds number turbulence, we comment on the parameter mapping:

- (17) compares the active and polymeric stresses which will lead to the same forces if the activity coefficient, $\zeta = -\frac{\mu_p}{\tau_p} \text{tr}(\mathbf{C})$. Importantly the correspondence holds for $\zeta < 0$, corresponding to contractile activity that exerts an active stress returning

the nematic system to an isotropic configuration, just as the elastic stress returns the polymers to an isotropic, unstretched state. As expected, higher $\text{tr}(\mathbf{C})$, i.e. more elongated polymers, and shorter relaxation times, τ_p , correspond to higher activities.

- (15) is the mapping of the molecular field, which encodes relaxation to equilibrium. The mapping is physically sensible for a positive quadratic term in the free energy ((8)), $A > 0$, and hence an equilibrium state where there is no nematic alignment, $S = 0$. It is known that such an isotropic equilibrium state is stable to contractile activity in the absence of imposed flow [40], corresponding to the occurrence of polymer dynamics only under flow.

- Finally, (16) shows that the diffusion of stretched polymers corresponds to Frank elasticity, which describes deformations of the orientational order in liquid crystals and active nematics. In the polymer literature, ϵ is typically chosen as small as possible while maintaining numerical stability on the premise that this limit best represents physically realistic polymer behavior. However its value is known to influence quantitative features of the flow [34–36]. By contrast, in active nematic systems, the elastic constant K is an important contributor to the physics: in particular the active length scale, which describes the size of vortices and of nematic domains in the active turbulent state $\sim \sqrt{K/\zeta}$ [24, 25].

D. Non-dimensionalizing the equations of motion

Our numerical results are obtained by solving (1) for the conformation tensor \mathbf{C} and (3) for the velocity field \mathbf{u} . It is helpful to non-dimensionalize these equations as

$$Re \frac{D\mathbf{u}}{Dt} = -\nabla P + \nabla^2 \mathbf{u} + \frac{\mu_p}{\mu_s} \frac{1}{Wi} \nabla \cdot (\mathbf{C} - \mathbf{I}) + Re_F \hat{\mathbf{F}}, \quad (18)$$

$$\frac{D\mathbf{C}}{Dt} = \mathbf{S}_C - \frac{1}{Wi} (\mathbf{C} - \mathbf{I}) + \frac{1}{Pe} \nabla^2 \mathbf{C}, \quad (19)$$

where we do not explicitly distinguish the dimensionless fields to avoid cumbersome notation. The dimensionless control parameters, the Reynolds number Re , the flow Reynolds number Re_F , the Weissenberg number Wi and the Péclet number Pe are, respectively, defined as

$$Re = \frac{\rho U L}{\mu_s}, \quad Re_F = \frac{\rho F L^2}{\mu_s U}, \quad \frac{1}{Wi} = \frac{L}{\tau_p U}, \quad Pe = \frac{UL}{\epsilon}, \quad (20)$$

where U and L are characteristic velocity and length scales. Note that in the active nematic limit of constant

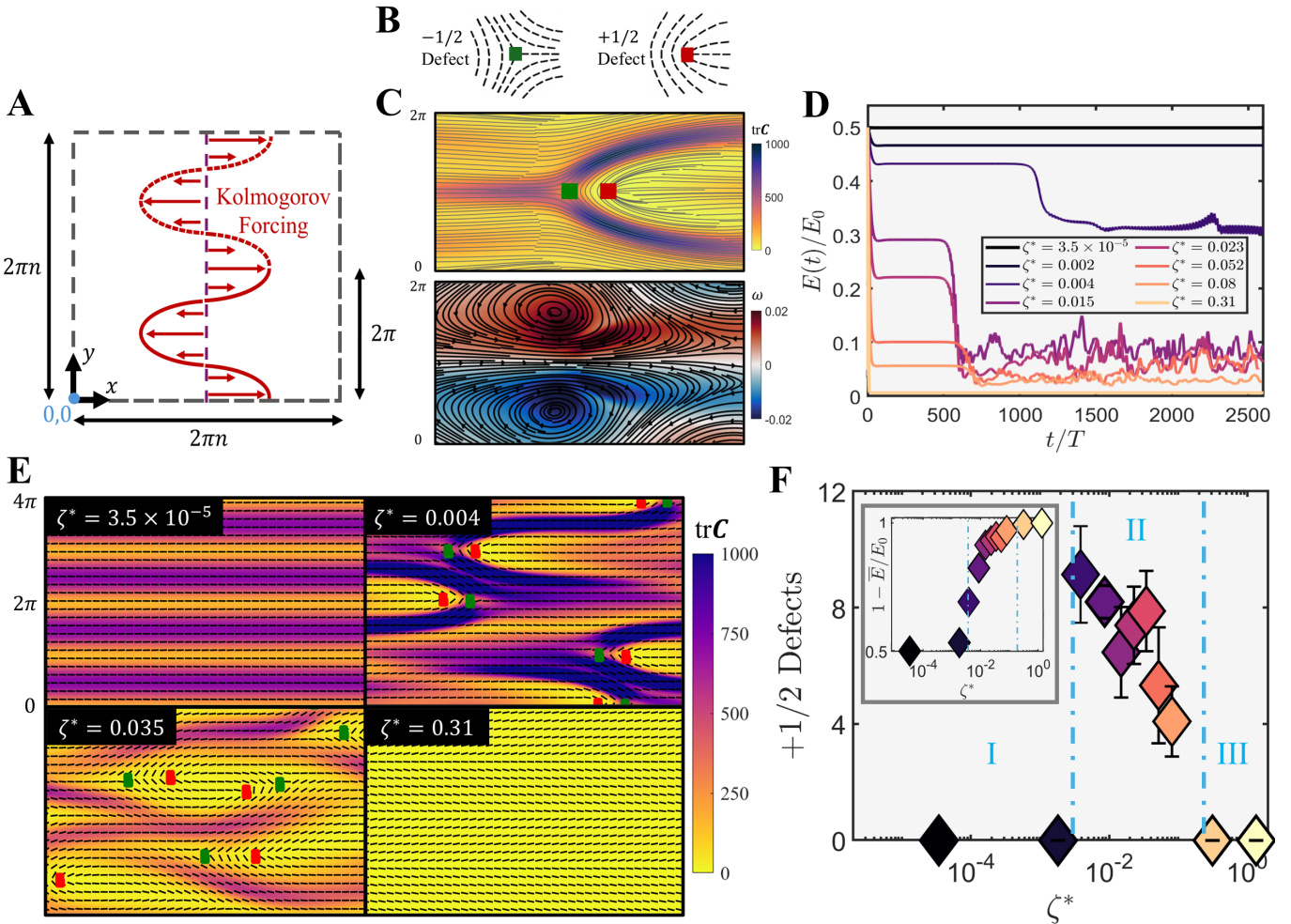


FIG. 1. **Elastic turbulence reveals $\pm 1/2$ topological defects in the polymer director field.** (A) Schematic of the fully periodic 2D Kolmogorov flow setup with sinusoidal forcing (shown in red) applied along the x -axis. The forcing wavelength is 2π and the number of wavelengths is controlled by the integer n . (B) Schematic illustration of half-integer topological defects, namely, a comet-like $+1/2$ defect (red marker) and a trefoil-like $-1/2$ defect (green marker). (C) Snapshot of the characteristic arrowhead structure observed for elastic turbulence over a single forcing wavelength $y = [0, 2\pi]$. Top: Director field superimposed on top of the $\text{tr}(\mathbf{C})$ field, revealing that each arrowhead corresponds to a half-integer defect pair. Bottom: Arrowheads are accompanied by strong secondary flows, as shown by the vorticity-field contours overlaid with velocity streamlines that represent the deviation from the background Kolmogorov flow. (D) Time series of the spatially averaged kinetic energy normalized by the kinetic energy of the fixed-point laminar flow, i.e., $E(t)/E_0 = \langle \mathbf{u}^2 \rangle / U^2$ for different levels of dimensionless activity ζ^* . (E) Representative snapshots of the $\text{tr}(\mathbf{C})$ field with the director field \mathbf{n} superimposed for $x = [0, 4\pi]$ and $y = [0, 4\pi]$. (F) Number of $+1/2$ defects for different ζ^* in the statistical steady-state. The inset shows the temporally averaged flow resistance $1 - \bar{E}/E_0$ for the same values of ζ^* . In both plots, we observe a non-trivial sequence of transitions with increasing ζ^* : I. passive Kolmogorov flow with no defects, II. a defect-rich regime accompanied by increasing flow resistance, III. a defect-free, high-resistance jammed state.

$\text{tr}(\mathbf{C})$, (17) can be used to define a dimensionless activity ζ^* as

$$\frac{\mu_p}{\mu_s} \frac{1}{Wi} = \frac{\zeta L}{\mu_s U} \equiv \zeta^*. \quad (21)$$

Hence, in terms of non-dimensional variables, the viscosity ratio normalized by the Weissenberg number acts as the system's activity parameter in polymeric turbulence.

II. RESULTS

A. Simulation details

We conduct numerical simulations of the two-dimensional Kolmogorov flow with input energy along $\hat{\mathbf{x}}$,

$$F(y) = F_{KF} \cos(y), \quad (22)$$

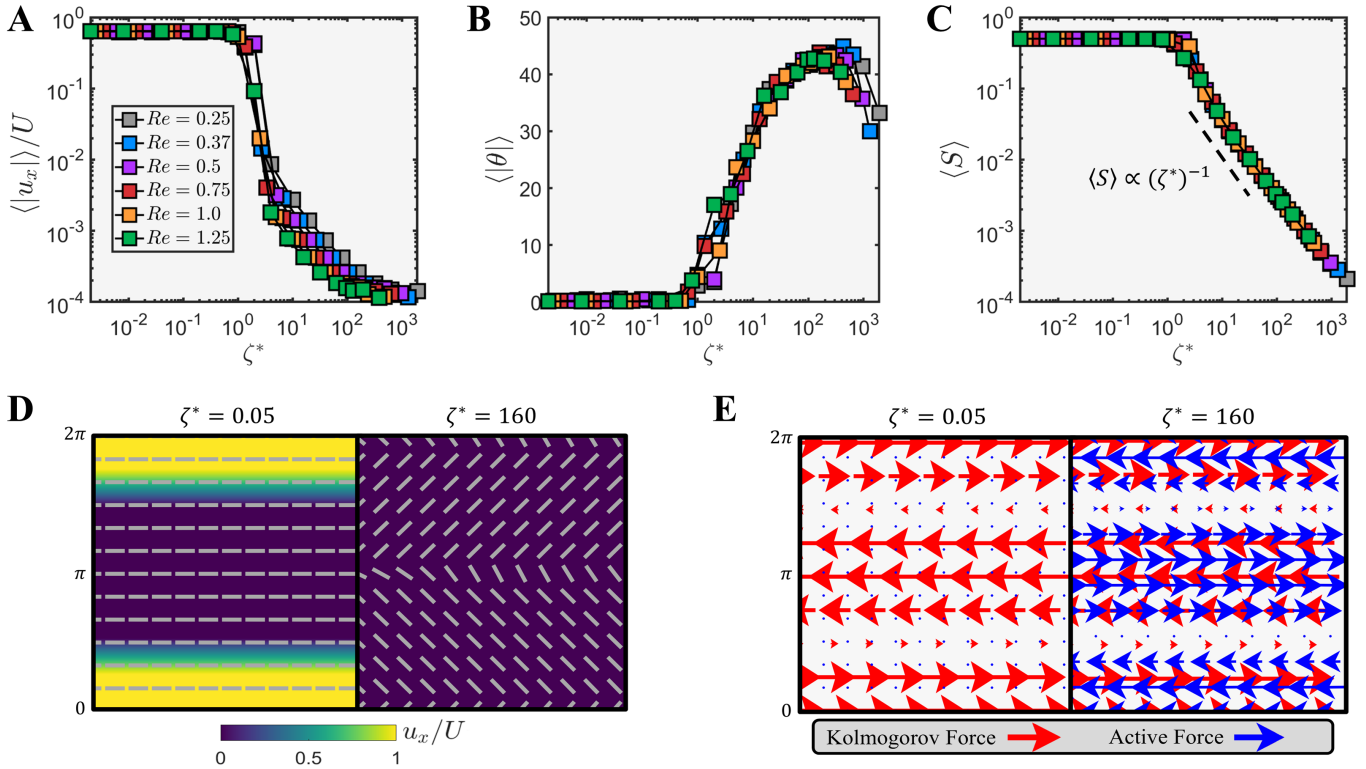


FIG. 2. Spontaneous flow instability in inextensible polymers (active nematics) with a constant contractile activity coefficient. Simulations are performed across the $Re - \zeta^*$ phase space for the spatially averaged (A) normalized streamwise velocity magnitude $\langle |u_x| \rangle / U$, (B) angle between the director and the x -axis, $\langle |\theta| \rangle$, and (C) order parameter magnitude $\langle S \rangle$. A rapid change in behavior occurs at $\zeta^* \approx 10^0$, marking the point at which contractile active stresses begin to impact the dynamics. (D) This behavior is further illustrated in the streamwise-velocity contour plots comparing the low ($\zeta^* = 0.05$) and high ($\zeta^* = 160$) activity regimes. At low activity, the system recovers the passive Kolmogorov forcing laminar solution, with a well-ordered director field (white bars) aligned in the streamwise direction. As the activity is increased, the flow is strongly reduced and the director field exhibits pronounced splay. (E) This jammed state corresponds to contractile active forces (blue) that are of comparable magnitude to the imposed Kolmogorov forcing (red), but opposite in direction, resulting in a near-complete cancellation of the mean flow.

where F_{KF} is the forcing amplitude and we have chosen the unit of length so that the forcing wavelength is 2π . As illustrated in Fig. 1A, the domain is of size $[0, 2\pi n] \times [0, 2\pi n]$ with fully periodic boundary conditions, where the integer n defines the number of wavelengths applied to the system. By using the amplitude of the fixed-point Newtonian laminar velocity (i.e., $\mu_p = 0$) $U = \rho F_{KF} L^2 / \mu_s$, we obtain the turnover time $T = \mu_s / \rho F_{KF} L$.

We take the flow to be in the low-inertia elastic turbulence regime, and, as such, keep the Reynolds number $Re < \sqrt{2}$ [41, 42]. The diffusion coefficient is fixed by setting $Pe \approx 2.5 \cdot 10^2$, and the activity is controlled either by varying the free parameter $\text{tr}(\mathbf{C})$ in the active nematic limit or μ_p for extensible polymers. The flow aligning parameter is chosen to be $\lambda = 1$ corresponding to the Oldroyd-B model commonly used to describe the evolution of polymers [28, 37]. We solve the governing equations using a hybrid lattice Boltzmann–finite-difference method [43], as detailed in **Materials and Methods**.

B. Director field and topological defects in elastic turbulence

We begin by outlining the physics of active turbulence and then draw analogies for the investigation of elastic turbulence. Contractile active turbulence is initiated by the instability of nematic order to splay deformations in the nematic director field [44]. In the fully developed turbulent state, spatial gradients in both the direction and magnitude of the nematic order parameter \mathbf{Q} generate the forces that drive the flow (see (10)). A defining feature of active turbulence is the appearance of the distinctive director patterns shown in Fig. 1B, termed topological defects, and labelled by their topological charge $\pm 1/2$. The defects are continually created and annihilated in pairs, leading to a steady state defect distribution. They are advected by the background active flow; in addition, the polar symmetry of the $+1/2$ defects means that they are self-propelled by the flows created by local director distortions.

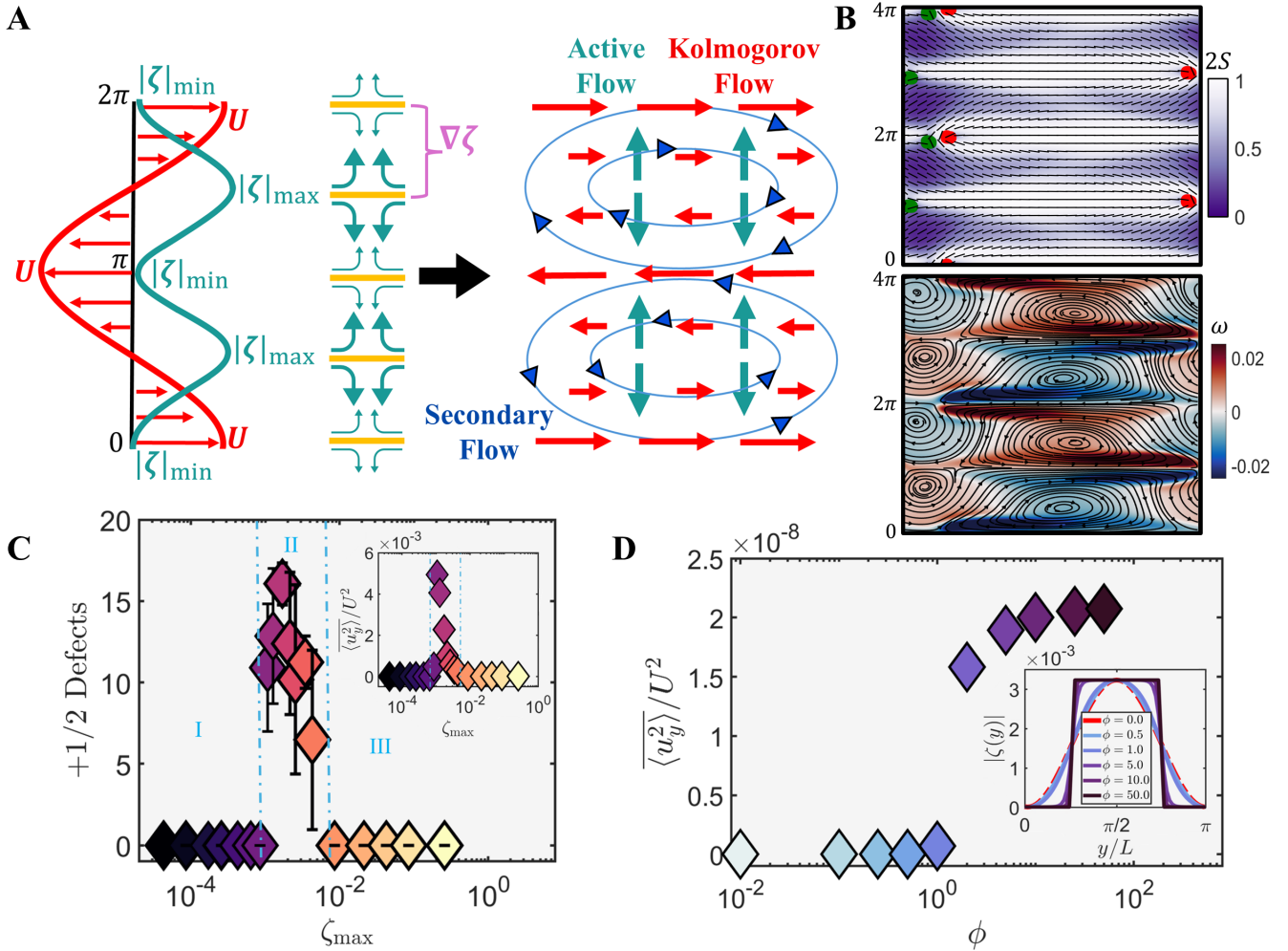


FIG. 3. Activity gradients in inextensible polymers give rise to a transverse instability and topological defects. (A) A spatially varying sinusoidal activity coefficient is defined for the Kolmogorov forcing problem (see Materials and Methods). Inextensible polymers then generate active stresses, which can create flows in the transverse direction. As a result each forcing wavelength develops a pair of coherent, counter-rotating vortices. (B) Representative snapshots obtained from numerical simulations at $\zeta_{\max} = 0.0039$. Top: Contour plot of the order parameter S with the director field superimposed. $+1/2$ and $-1/2$ topological defects are marked in red and green respectively. Bottom: Vorticity field with the velocity streamlines superimposed. (C) Number of $+1/2$ defects for different ζ_{\max} in the statistical steady-state. The inset shows the corresponding temporally averaged mean secondary-flow strength, $\langle u_y^2 \rangle / U^2$. Notably, the transverse instability is associated with the formation of topological defects. (D) To demonstrate the role of $\nabla\zeta$, we conduct additional simulations at $\zeta_{\max} = 0.006$ and control the steepness ϕ (Materials and Methods) of the imposed activity profile. The transition into secondary flows is enhanced as the sinusoidal activity profile transitions into a sharper "step-like" response. The inset shows the activity profile $|\zeta(y)|$ across half a forcing wavelength for different ϕ values.

Given the connection between active and elastic turbulence, a natural question is whether the director field and topological defects might be used to help characterize and understand elastic turbulence. To investigate this, we solve the full polymer equations of motion, (18) and (19), with Kolmogorov forcing, (22), in the geometry illustrated in Fig. 1A. Fig. 1D shows the time series of the dimensionless spatially averaged kinetic energy $E(t)/E_0 = \langle \mathbf{u}^2 \rangle / U^2$ for different dimensionless activity coefficients ζ^* . For small values of activity the system converges to steady laminar Kolmogorov flow, whereas intermediate values

generate strong time-dependent oscillations in the kinetic energy, characteristic of elastic turbulence. Larger values of the activity lead to a jammed response where the flow field in the channel is close to zero.

Typical snapshots of the late time behavior, for increasing values of the dimensionless activity ζ^* corresponding to each of these behaviors, are shown in Fig. 1E for $x \in [0, 4\pi]$ and $y \in [0, 4\pi]$, and corresponding animations are provided in Movies S2, S3, S4, and S5. In addition to plotting $\text{tr}(\mathbf{C})$, the polymer elongation, which is the variable commonly used to study the polymer microstructure,

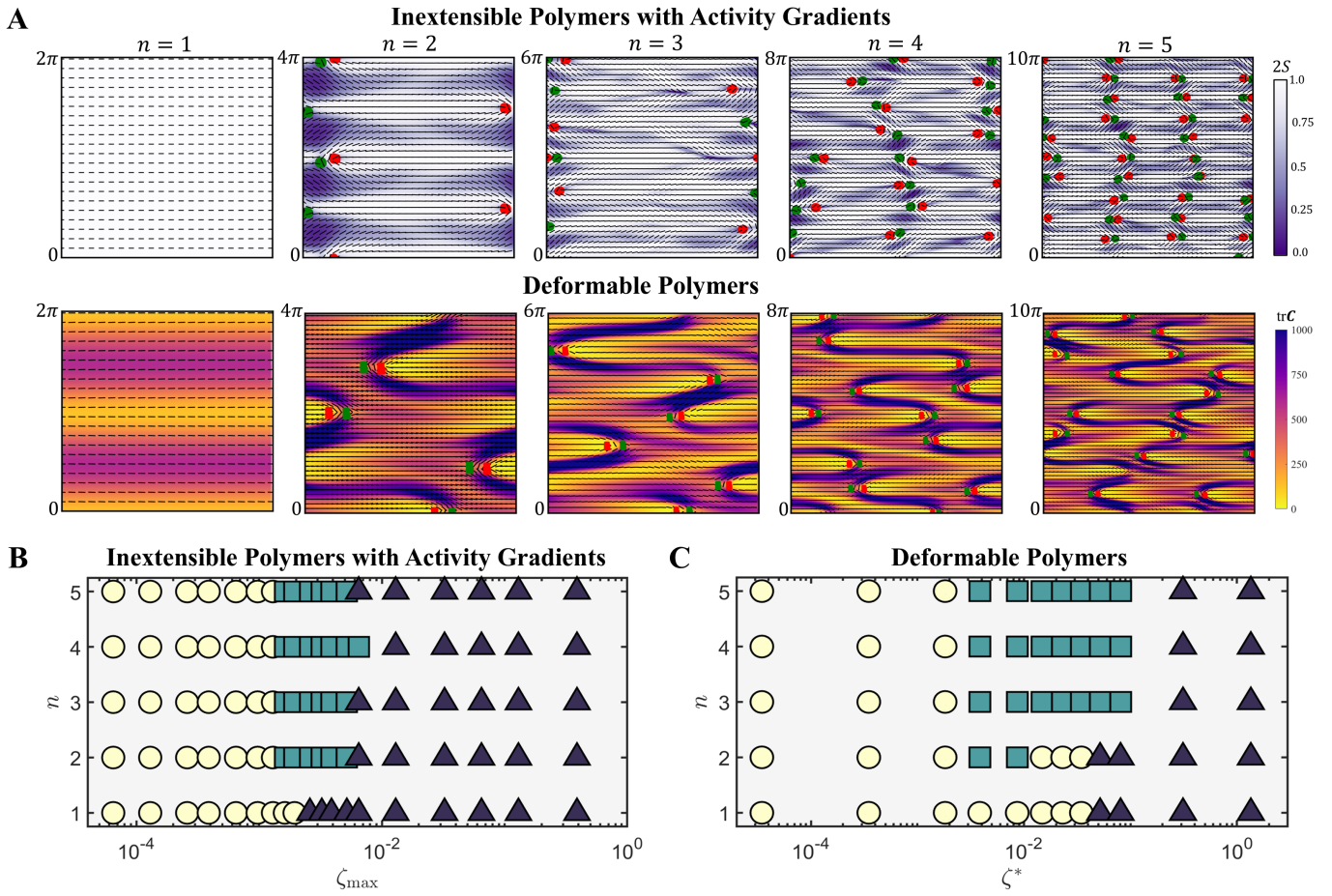


FIG. 4. Comparing inextensible polymers (active nematics) with activity gradients to polymers that can stretch. (A) Contour plots for (top row) the degree of alignment measured by S for active nematics with spatially varying activity and (bottom row) $\text{tr}(\mathbf{C})$ for deformable polymers where the activity gradient is space and time dependent. In both cases, the director field \mathbf{n} is superimposed with $+1/2$ (red) and $-1/2$ (green) topological defects. Snapshots are provided for different square domain sizes n . (B-C) Diagrams showing the final states identified across different domain sizes and activity levels for the active nematics and polymeric fluids, respectively. In both plots, three distinct dynamical regimes emerge. At low activity and small domain size, the system exhibits passive Kolmogorov flow with no defects (yellow circles). For moderate activity and sufficiently large domains, secondary flows develop, and defect pairs appear (green squares). At high activity, the system transitions into a jammed state characterized by the absence of defects (purple triangles).

we also recorded the additional information contained in **C**. This includes the associated director field, defined by the principal eigenvector of \mathbf{C}^* , as well as the locations of $\pm 1/2$ topological defects identified in this field. Note that \mathbf{C} and \mathbf{C}^* share the same eigenvectors, and the director field therefore indicates the orientation of elongated polymers.

At low activity, the polymers are stretched and aligned along the x -axis. There is no splay distortion in the director field, and hence no active flow, thus the velocity profile remains that of the Kolmogorov forcing in a Newtonian fluid. At intermediate activity, $\zeta^* = 0.004$, we see the appearance of the long-lived arrowhead structures in $\text{tr}(\mathbf{C})$, which are well-documented features of elastic turbulence [9–11]. Strikingly, each arrowhead is associated with a pair of topological defects in the director field (Fig. 1C,

Movie S1). We note that these are located in the vicinity of, but do not coincide with, the flow stagnation points in the co-moving frame identified in [45].

Further increasing activity to $\zeta^* = 0.035$ tends to destabilize the pattern of arrowheads, creating secondary filament structures [46] (Movie S4). However, long-lived arrowhead structures remain, albeit that they are less ordered. The arrowheads continue to correspond to bound defects [31], and the disappearance and reappearance of arrowheads correspond to the annihilation and birth of defect pairs.

Finally, and unexpectedly, we found that a further increase in activity to $\zeta^* = 0.31$, leads to a state where the velocity field is close to zero everywhere (Movie S5).

Fig. 1F shows the number of $+1/2$ defects as a function of the activity: defects form at intermediate activities

where they are associated with arrowheads and turbulent flows, while no defects are observed at low or high activities, coinciding with regimes of minimal and maximal flow resistance, respectively (see inset).

To investigate this behavior in more detail, we first solve the polymer equations of motion [(18) and (19)] in the active nematic limit by keeping $\text{tr}(\mathbf{C})$ constant. We then introduce spatial gradients in $\text{tr}(\mathbf{C})$ that are fixed in time, representing spatially varying, time-independent activity, and finally compare these results to the solutions of the full polymer equations.

C. Constant activity for inextensible polymers: the active nematic limit

Holding $\text{Tr}(\mathbf{C})$ constant, to correspond to the active nematic limit, we solve the equations of motion in Kolmogorov flow. In this system, we observe no transverse instabilities, obtaining a 1D flow field, with no velocity along y .

Fig. 2A-C show, respectively, how the spatially averaged magnitude of the scaled velocity, $\langle |u_x| \rangle / U$, the magnitude of the angle between the nematic director and the x -axis, $\langle |\theta| \rangle$, and the nematic order parameter, $\langle S \rangle$, vary with ζ^* . (The nematic order parameter S is the largest eigenvalue of \mathbf{C}^* and indicates the nematic ordering of stretched polymers.) In each case in Fig. 2A-C, there is a rapid crossover between the force dominated ($\zeta^* < \mathcal{O}(1)$) and activity dominated ($\zeta^* > \mathcal{O}(1)$) regimes. Further, in each case there is a data collapse for varying Re , showing that the physics is controlled by a balance between the Kolmogorov forcing and the activity.

Figs. 2D and E show the variation of the director field across the channel, and the forces which result in this behavior, in the flow dominated (left panels) and activity dominated (right panels) regimes. At low activities, the Kolmogorov forcing (red arrows in Figs. 2E) dominates, and the scaled velocity magnitude is equal to $2/\pi$, as expected for a sinusoidal flow profile. The polymer configuration is independent of the activity, emphasising the dominance of the imposed flow. For the choice of flow aligning parameter $\lambda = 1$, polymers lie along the x -axis (Fig. 2A and D) and the nematic order parameter averaged across the channel takes the constant value $\langle S \rangle = 0.5$, corresponding to strong nematic ordering of stretched polymers (Fig. 2C).

Once the activity is sufficiently large, the aligned polymers undergo the well-known active contractile instability [20, 47–49] to give a splayed director configuration (Fig. 2D), with the splay increasing with increasing activity (Fig. 2A). The resulting contractile stresses create a flow (blue arrows in Figs. 2E) which opposes the Kolmogorov forcing and the net velocity in the channel starts to decrease (Fig. 2B). As the flow decreases, it becomes less effective at stretching and aligning the polymers, so

the nematic order parameter, $\langle S \rangle$, also decreases (Fig. 2C), approximately linearly with ζ^* . In the limit that activity dominates the Kolmogorov flow, there is cancellation between the active and Kolmogorov forces resulting in no net flow in the streamwise direction.

D. Spatial activity gradients for inextensible polymers: origin of transverse instability

The development of velocities along the y -axis, is needed to drive a transition from Kolmogorov's bidirectional flow state to elastic turbulence. We found no evidence of such an instability in the simulations in which activity was held constant. Previous numerical work [10, 45, 50] has demonstrated that elastic turbulence is marked by thin regions of highly deformed polymers, reflected in localized variations of $\text{tr}(\mathbf{C})$, which in the active nematic limit, corresponds to changes in activity. Therefore, to investigate a possible role of activity gradients in driving the transverse instability, we varied the activity along y according to the modified hyperbolic tangent profile,

$$\zeta(y) = \frac{\zeta_{\max} + \zeta_{\min}}{2} - \frac{\zeta_{\max} - \zeta_{\min}}{2} \frac{\tanh(\phi \cos(4\pi y))}{\max |\tanh(\phi \cos(4\pi y))|}, \quad (23)$$

where $\phi \rightarrow 0$ recovers a pure sinusoidal profile, while finite values of ϕ produce progressively steeper variations in $\zeta(y)$ (inset of Fig. 3D). Note that the activity has half the wavelength of the Kolmogorov flow profile so that there is a maximum in the activity to coincide with positions of maximum strain rate in the flow, as shown in Fig. 3A. Such activity variation is natural in polymeric fluids when subjected to the Kolmogorov flow as $\text{tr}(\mathbf{C})$ is maximal (minimal) where the velocity gradient is maximal (minimal).

This situation is not equivalent to the full polymer simulations because, although the activity or equivalently the polymer extension, $\text{tr}(\mathbf{C})$, varies in space, it is constant in time. Yet, for suitable choices of parameters, discussed in more detail below, we observe the pattern of flow vortices and topological defects, shown in Fig. 3B and Movie S6. The mechanism behind this is illustrated schematically in the right-hand panel of Fig. 3A. Forces from the activity gradients (i.e. polymers elongated to varying degrees) produce flows along y which, together with the constraint of incompressibility, lead to vortices. Defects form along the lines where the Kolmogorov flow gradient is zero and there is a large mismatch in director angles along the y -direction. A pair of counter-rotating vortices, reminiscent of the flow signature of arrowheads, is formed on either side of these defects.

To investigate the role of varying activity further, in Fig. 3C we plot the number of defects as a function of ζ_{\max} . The inset of the figure shows the corresponding normalized, time-averaged, mean square secondary flow

for fixed $\phi = 0$. We can identify the same three regions as for the full polymer equations (compare Fig 1E). Region I corresponds to streamwise Kolmogorov flows, with no topological defects, Region II corresponds to the development of vortices and topological defects, and Region III is a jammed state with no topological defects. In Fig. 3D we vary the steepness of the activity profile for fixed ζ_{min}, ζ_{max} , demonstrating that the activity gradient is an important control parameter for the transverse instability – the steeper the profile, the stronger the resulting flows along y .

E. Comparing inextensible polymers (active nematics) with activity gradients to deformable polymers

Recent work [11] simulating elastic turbulence using the Kolmogorov forcing has demonstrated that the transverse instability and consequent patterns formed in dilute polymer suspensions depend on the size of the simulation box. We use this observation as a basis for a further comparison of the dynamics of active nematics with spatially varying activity to a system described by the full polymeric equations of motion where the effective activity varies in both space and time.

Snapshots comparing the two cases in square simulation boxes, for different values of n , the number of Kolmogorov wavelengths across the box, are shown in Fig. 4A (see Fig. S1 in the SM for the corresponding flow fields). We observe the formation of topological defects and associated secondary flows only in sufficiently large domains, i.e., $n \geq 2$. The pattern of topological defects is qualitatively similar in the two cases, suggesting that the same instability is responsible for the transverse flows. However, as expected, the details of the pattern varies as $\text{tr}(\mathbf{C})$ is allowed to vary with time in the snapshots in the lower panel, that correspond to the polymeric system. This leads to the formation of the coherent structures which comprise arrowheads, distinctive regions of large $\text{tr}(\mathbf{C})$ associated with a bound defect pair.

As a second way to compare the two systems, we present phase plots showing the long-time dynamical states as n is varied. Fig. 4B shows results for the active nematic as a function of ζ_{max} for the purely sinusoidal profile (i.e., $\phi \rightarrow 0$) with fixed $\zeta_{min} = -1.3 \times 10^{-5}$. Fig. 4C shows a similar plot for polymers, where now the control parameter is the effective activity ζ^* . There is a striking similarity between the two cases: the transverse instability leads to a vortex lattice and topological defects at intermediate activities, sandwiched between the Kolmogorov flow state and the activity-jammed state, as n is increased.

III. DISCUSSION

The primary aim of this paper has been to describe the connection between low Reynolds number turbulence in driven dilute polymer suspensions and contractile active nematics. We show that both systems correspond to the same equations of motion if the active nematic is isotropic in the absence of activity, and is deformable. This suggests that the topological defects and the nematic director field that control active turbulence may provide useful new ways to interpret elastic turbulence. In particular, we show that the arrowheads that characterize turbulence in polymeric fluids can be interpreted as long-lived coherent states formed around topological defect pairs which appear at positions which correspond to large splay deformations in the director field.

Conversely, the polymer turbulence literature will provide promising yet unexplored avenues for studying active nematics. Because contractile active nematics, which are isotropic in the passive limit, have no active dynamics in the absence of an imposed flow they have received little attention so far. Motivated by our mapping, we studied the behavior of these systems in the Kolmogorov flow field. We found that when imposed flow dominates activity, the nematogens are aligned by the flow. However, at sufficiently large activities, they quickly crossover to a splay configuration which creates stresses that oppose the Kolmogorov forcing. As a result the velocity, and hence the nematic order, decreases leading to a jammed state.

A similar instability, from no flow to spontaneous laminar flow, driven by the usual active nematic bend or splay instability, is well known in channel-confined extensile active nematics [20, 47–49], and in contractile systems with thermodynamically-imposed nematic ordering. At higher activities in these models, there is a transition to a line of flow vortices arranged along the channel [51]. In the active paranematic under Kolmogorov flow considered here, we saw no evidence of such a transition with increasing, constant, activity. We explain this by noting that activity gradients must be sufficiently strong to drive a transition to the vortex state, but before this happens the activity becomes large enough to destroy the ordering and flow-alignment of the nematic director field.

To drive a transverse instability and form secondary flow structures, we needed to either add activity gradients along the y -axis in the active nematic simulations, or solve the full polymer equations. In both cases, this resulted in vortex formation and the production of topological defects for values of activity close to that corresponding to the transition from Kolmogorov to activity-dominated flow. Moreover, the results for the two models depended in the same distinctive way on the size of the simulated domain. These similarities suggest that the center mode instability [11], implicated in initiating the transverse flow in polymers, may also be relevant to the transition from

laminar to vortical flow in active nematics, an interesting direction for future research. By contrast, arrowheads formed only when the activity variation had the time dependence encoded in the dynamical equation for the polymer extension, $\text{tr}(\mathbf{C})$.

In formulating the mapping we ignored the elastic backflow stress that appears in the equations of active nematics. To leading order this is given by $\lambda A \mathbf{Q}$ which is negligible when A is small or equivalently when $\text{tr}(\mathbf{C})$ is large ((15)). The polymeric stress is also a backflow term, but this is $\propto \text{tr}(\mathbf{C})$, which typically increases with flow strength, leading to large polymeric stresses. The order-of-magnitude comparability between the polymeric stress and the dominating active stress term is the fundamental reason behind (17).

There are many directions in which to further investigate the polymer – active nematic mapping. For example, confluent epithelial cell layers and tissues, which are deformable active nematics, can be modeled using the polymer equations of motion. Polymer dynamics in the absence of an imposed flow can be initiated by using an effective extensile activity or a free energy term that forces the polymers to remain in a state with $\mathbf{C} \neq \mathbf{I}$. This provides a continuum description of active polymers which have recently received considerable attention in the literature [52]. It would also be interesting to move beyond the low Reynolds number regime and consider deformable active nematics in the elasto-inertial regime, to consider polymeric turbulence in 3D in the context of nematic disclination lines, and to study whether more complex representations of polymer rheology can be cast into an active nematic framework.

Lastly, in contrast to polymer molecules, many experimentally studied active systems are composed of colloidal-scale constituents, which allow direct visualization of the evolving microstructure. Our mapping between polymeric turbulence and active turbulence therefore offers a potential route to testing theoretical and computational findings—particularly those concerning microstructural evolution—that are difficult to access experimentally in dilute polymer solutions.

IV. MATERIALS AND METHODS

A. Numerical Method

Equations (18) and (19) are solved using a numerical solver developed in-house, comprising of the lattice Boltzmann (LB) method coupled with a high-order finite-difference scheme [see [43]], which was applied in our previous investigations of elastic turbulence flow problems [35, 53–57]. The hydrodynamic equations are solved using a single-relaxation-time (SRT) LB method on a standard D2Q9 lattice. The polymer field is resolved using a high-resolution finite-difference scheme, where spatial

gradients are solved using a second-order central difference scheme, while a fourth-order Runge-Kutta scheme is applied for the temporal evolution. Careful attention is given to the advection term in (19), which is discretized using the high-resolution Kurganov-Tadmor scheme [58]. To prevent the rapid growth of Hadamard instabilities [59], we further conserve the symmetric positive-definite (SPD) properties of the conformation tensor $\mathbf{C} \geq 0$ by applying the Cholesky-log decomposition [60]. Full numerical details of the solver can be found in Dzanic *et al.* [43].

In terms of simulation parameters, we use LB units, where the discrete space and time steps are chosen as unity, and all quantities can be expressed in dimensionless form. Both rigid and extensible polymers are assumed to be flow-aligning particles with $\lambda = 1$, which produce contractile force dipoles, hence $\zeta < 0$. Following previous work [56, 57], we discretize the domain using $L = 128/2\pi$, with further refinement to $L = 256/2\pi$ yielding indistinguishable results and confirming numerical convergence. Unless specified otherwise, all simulations are performed with the parameters, $n = 4$, $Re = 1$, $Re_F = 1$, $Wi \approx 28.5$, and $Pe \approx 2.5 \cdot 10^2$.

Simulations are commenced under an initially isotropic, quiescent flow state where $\mathbf{C} = \mathbf{I}$ and $\mathbf{u} = 0$. To simulate elastic turbulence, a small perturbation $\boldsymbol{\delta}$, a random Gaussian (normally distributed) noise in the order of $\mathcal{O}(10^{-6})$, is introduced to the initial velocity field $\mathbf{u}(t = 0, \mathbf{x}) + \boldsymbol{\delta}$, thereby seeding the instability. Fully periodic boundary conditions are employed in both spatial directions to model the Kolmogorov flow configuration.

B. Controlling Activity Gradients

To investigate the role of spatial activity gradients $\nabla\zeta$ on the instability mechanism, we define a sinusoidal activity, which is constant in time,

$$\zeta(y) = \frac{(\zeta_{\max} + \zeta_{\min})}{2} - \frac{(\zeta_{\max} - \zeta_{\min})}{2} \cos(4\pi y), \quad (24)$$

which periodically varies between ζ_{\min} and ζ_{\max} , with a wavelength half that of the Kolmogorov forcing. Throughout, we fix the minimum activity level at $\zeta_{\min} = -1.3 \times 10^{-5}$. In doing so, the contractile stress contribution from rigid polymers (i.e., $\text{tr}(\mathbf{C})$ held constant) becomes $\sigma_p \approx \zeta(y) \mathbf{C}^*$.

To elucidate the role of activity gradients in driving the transverse instability reported in the results, we systematically control the steepness of $\nabla\zeta$ using the modified hyperbolic tangent profile,

$$\zeta(y) = \frac{\zeta_{\max} + \zeta_{\min}}{2} - \frac{\zeta_{\max} - \zeta_{\min}}{2} \frac{\tanh(\phi \cos(4\pi y))}{\max |\tanh(\phi \cos(4\pi y))|}, \quad (25)$$

where $\phi \rightarrow 0$ recovers the pure sinusoidal profile, while finite values of ϕ produce a progressively step-like variation in $\zeta(y)$. We perform simulations across $\phi \in [0.01, 0.1, 0.25, 0.5, 1, 2, 5, 10, 25, 50]$ to systematically investigate the effect of gradient steepness on the transverse instability.

ACKNOWLEDGMENTS

We thank Rich Kerswell and Rahil Valani for fruitful discussions. V. Dzanic acknowledges the High-Performance Computing facilities at QUT. SPT acknowledges funding from the Royal Society and the Wolfson Foundation through a Royal Society Wolfson Fellowship and support from the Department of Science and Technology, India, under research grant CRG/2023/000169. JMY acknowledges support from the ERC Advanced Grant ActBio (funded as UKRI Frontier Research Grant EP/Y033981/1).

* v2.dzanic@qut.edu.au

† sumesh@iitm.ac.in

‡ julia.yeomans@physics.ox.ac.uk

[1] A. Groisman and V. Steinberg, *Nature* **405** (2000).

[2] V. Steinberg, *Annu. Rev. Fluid Mech.* **53**, 27 (2021).

[3] A. Groisman and V. Steinberg, *New J. of Phys.* **6** (2004).

[4] C. A. Browne and S. S. Datta, *Sci. Adv.* **7**, eabj2619 (2021).

[5] A. Groisman and V. Steinberg, *Nature* **410**, 905 (2001).

[6] C. A. Browne and S. S. Datta, *Proc. Natl. Acad. Sci. U.S.A.* **121**, e2320962121 (2024).

[7] S. S. Datta, A. M. Ardekani, P. E. Arratia, A. N. Beris, I. Bischofberger, G. H. McKinley, J. G. Eggers, J. E. López-Aguilar, S. M. Fielding, A. Frishman, M. D. Graham, J. S. Guasto, S. J. Haward, A. Q. Shen, S. Hormozi, A. Morozov, R. J. Poole, V. Shankar, E. S. G. Shaqfeh, H. Stark, V. Steinberg, G. Subramanian, and H. A. Stone, *Phys. Rev. Fluids* **7**, 080701 (2022).

[8] R. Singh, P. Perlekar, D. Mitra, and M. Rost, *Nat. Commun.* **15** (2024).

[9] J. Page, Y. Dubief, and R. R. Kerswell, *Phys. Rev. Lett.* **125**, 154501 (2020).

[10] A. Morozov, *Phys. Rev. Lett.* **129**, 017801 (2022).

[11] T. Lewy and R. R. Kerswell, *J. Fluid Mech.* **1007**, A55 (2025).

[12] J. Dunkel, S. Heidenreich, K. Drescher, H. H. Wensink, M. Bär, and R. E. Goldstein, *Phys. Rev. Lett.* **110**, 228102 (2013).

[13] C. Dombrowski, L. Cisneros, S. Chatkaew, R. E. Goldstein, and J. O. Kessler, *Phys. Rev. Lett.* **93**, 098103 (2004).

[14] Y. Peng, Z. Liu, and X. Cheng, *Sci. Adv.* **7**, eabd1240 (2021).

[15] T. Sanchez, D. Chen, S. Decamp, M. Heymann, and Z. Dogic, *Nature* **491**, 431–434 (2012).

[16] P. Guillamat, J. Ignés-Mullol, and F. Sagués, *Nat. Commun.* **8**, 564 (2017).

[17] A. Doostmohammadi, S. P. Thampi, T. B. Saw, C. T. Lim, B. Ladoux, and J. M. Yeomans, *Soft Matter* **11**, 7328 (2015).

[18] C. Blanch-Mercader, V. Yashunsky, S. Garcia, G. Duclos, L. Giomi, and P. Silberzan, *Phys. Rev. Lett.* **120**, 208101 (2018).

[19] T. B. Saw, A. Doostmohammadi, V. Nier, L. Kocgozlu, S. Thampi, Y. Toyama, P. Marcq, C. Lim, J. Yeomans, and B. Ladoux, *Nature* **544**, 212 (2017).

[20] R. Aditi Simha and S. Ramaswamy, *Phys. Rev. Lett.* **89**, 058101 (2002).

[21] R. Alert, J. Casademunt, and J.-F. Joanny, *Annu. Rev. Condens. Matter Phys.* **13**, 143 (2022).

[22] S. P. Thampi and J. M. Yeomans, *Eur. Phys. J. Spec. Top.* **225**, 651 (2016).

[23] S. P. Thampi, R. Golestanian, and J. M. Yeomans, *Phys. Rev. Lett.* **111**, 118101 (2013).

[24] S. P. Thampi, R. Golestanian, and J. M. Yeomans, *Europhys. Lett.* **105**, 18001 (2014).

[25] S. P. Thampi, R. Golestanian, and J. M. Yeomans, *Phil. Trans. R. Soc. A* **372**, 20130366 (2014).

[26] L. Giomi, M. J. Bowick, X. Ma, and M. C. Marchetti, *Phys. Rev. Lett.* **110**, 228101 (2013).

[27] L. Giomi, M. J. Bowick, P. Mishra, R. Sknepnek, and M. C. Marchetti, *Phil. Trans. R. Soc. A* **372**, 20130365 (2014).

[28] M. Alves, P. Oliveira, and F. Pinho, *Annu. Rev. Fluid Mech.* **53**, 509 (2021).

[29] A. N. Beris and B. J. Edwards, *Thermodynamics of Flowing Systems* (Oxford University Press, New York, 1994).

[30] V. Steinberg, *Phys. Rev. Lett.* **123**, 234501 (2019).

[31] M. Lellep, M. Linkmann, and A. Morozov, *Proc. Natl. Acad. Sci. U.S.A.* **121**, e2318851121 (2024).

[32] R. Alert, J. F. Joanny, and J. Casademunt, *Nat. Phys.* **16**, 682 (2020).

[33] M. Lellep, M. Linkmann, and A. Morozov, *J. Fluid Mech.* **959**, R1 (2023).

[34] A. Gupta and D. Vincenzi, *J. Fluid Mech.* **870**, 405–418 (2019).

[35] V. Dzanic, C. S. From, and E. Sauret, *Phys. Rev. E* **106**, L013101 (2022).

[36] S. R. Yerasi, J. R. Picardo, A. Gupta, and D. Vincenzi, *J. Fluid Mech.* **1000**, A37 (2024).

[37] J. Hinch and O. Harlen, *J. Non-Newtonian Fluid Mech.* **298**, 104668 (2021).

[38] H. A. Stone, M. J. Shelley, and E. Boyko, *Soft Matter* **19**, 5353 (2023).

[39] P. G. de Gennes and J. Prost, *The Physics of Liquid Crystals*, 2nd ed. (Oxford University Press, Oxford, 1995).

[40] S. Santhosh, M. R. Nejad, A. Doostmohammadi, and J. M. Yeomans, *Journal of Statistical Physics* **180**, 699 (2020).

[41] G. Boffetta, A. Celani, and A. Mazzino, *Phys. Rev. E* **71**, 036307 (2005).

[42] K. Gotoh and M. Yamada, *J. of the Phys. Society of Japan* **53**, 3395 (1984).

[43] V. Dzanic, C. S. From, and E. Sauret, *Comput. Fluids* **235**, 105280 (2022).

[44] S. Ramaswamy and M. Rao, *N. J. Physics* **9**, 423 (2007).

[45] A. Morozov, M. Lellep, D. Capocci, and M. Linkmann, *Narwhals and their blessings: exact coherent structures of elastic turbulence in channel flows* (2025), arXiv:2509.03175 [physics.flu-dyn].

[46] S. Berti and G. Boffetta, *Phys. Rev. E* **82**, 036314 (2010).

[47] R. Voituriez, J. F. Joanny, and J. Prost, *Europhys. Lett.*

70, 404 (2005).

[48] R. Voituriez, J. F. Joanny, and J. Prost, *Phys. Rev. Lett.* **96**, 028102 (2006).

[49] S. A. Edwards and J. M. Yeomans, *Europhys. Lett.* **85**, 18008 (2009).

[50] J. R. King, R. J. Poole, C. P. Fonte, and S. J. Lind, *J. Fluid Mech.* **1020**, A2 (2025).

[51] T. N. Shendruk, A. Doostmohammadi, K. Thijssen, and J. M. Yeomans, *Soft Matter* **13**, 3853 (2017).

[52] Y. Zhang and W. Tian, *J. Phys.: Condens. Matter* **37**, 143002 (2025).

[53] V. Dzanic, C. From, and E. Sauret, *J. Fluid Mech.* **937**, A31 (2022).

[54] V. Dzanic, C. S. From, A. Gupta, C. Xie, and E. Sauret, *Phys. Fluids* **35**, 023105 (2023), <https://doi.org/10.1063/5.0138184>.

[55] V. Dzanic, C. S. From, and E. Sauret, *Phys. Rev. Fluids* **9**, 063301 (2024).

[56] C. S. From, V. Dzanic, V. Niasar, and E. Sauret, *J. Fluid Mech.* **1017**, R1 (2025).

[57] V. Dzanic, C. S. From, and E. Sauret, *PNAS Nexus* **4**, pgaf231 (2025).

[58] A. Kurganov and E. Tadmor, *J. Comput. Phys.* **160**, 241 (2000).

[59] R. Sureshkumar and A. N. Beris, *J. Non-Newtonian Fluid Mech.* **60**, 53 (1995).

[60] T. Vaithianathan and L. R. Collins, *J. of Comput. Phys.* **187**, 1 (2003).